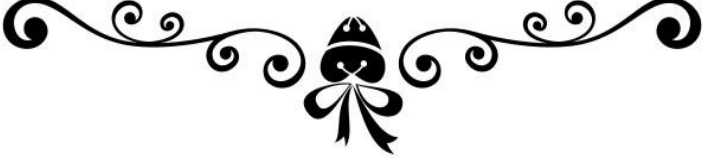




Chapter-3

Band gap tuning and studies of photo-ferroelectric properties of PbTiO_3



3.1 Introduction

PbTiO₃ is an extensively studied displacive ferroelectric material with very high room temperature spontaneous polarization ($P_S = 59 \mu\text{C}/\text{cm}^2$) [21, 123-125] due to very large tetragonality (~ 1.06) [126]. The ferroelectric ordering in displacive ferroelectrics is coupled to strain in the lattice and a larger crystallographic distortion leads to higher polarization [78]. Thus, if tetragonality of PbTiO₃ is enhanced or retained, while chemical substitution/doping to decrease the band gap, the polarization will not decrease. Cationic displacement at the B-site is the fundamental cause of driving ferroelectricity in many perovskite ferroelectrics [56], and is caused by the hybridization of the 3d-orbitals of B-site cations with the 2p-orbitals of the oxygen, that are also involved in forming the conduction and valence bands respectively. Recent reports in literature suggest that, substitution at the Ti-site in the perovskite PbTiO₃ with many other transition-metal (TM) ions enhances the covalent character in the bonding, making it less ionic with oxygen and can reduce the bandgap [54]. It has been earlier reported that 5% substitution of Ni, Fe and Mn-ions at Ti site in PbTiO₃ reduces band gap from 3.30 eV to 2.51, 2.53 and 2.62 eV respectively [15]. Further, the Mn-Nb co-substitution at Ti site in BaTiO₃ reduces the band gap from 3.18 to 1.66 eV [22]. The (KNbO₃)_{1-x}(BaNi_{1/2}Nb_{1/2}O₃)_x solid solution, where two transition metals Ni and Nb were introduced at the B-site, shows wide tunability of band gap from 1.18 eV to 3.8 eV with changing composition [29]. The encouraging experimental finding for PbTiO₃ was reported by [26]. In the samples prepared by solid state method, W. Zhou et. al. showed a band gap reduction of PbTiO₃ up to 2.42 eV, by 33% Ni substitution at the Ti-site [127]. Unoccupied d-orbital of Ti⁴⁺ allows for a stable hybridized bond with the apical O²⁻ ions favouring ferroelectric behaviour. The substitution of uncurbed Ti by another metal, possessing partially filled d-orbital is undesirable as it can weaken the

ferroelectric behaviour. To address these concerns, we have selected PbTiO_3 as the parent compound which has very high saturation polarization and small substitution at the Ti-site for tuning the band gap is not going to deteriorate much the ferroelectric behaviour of the resulting compound. Further, Mo has been selected as substituting element, which is relatively more electronegative (electronegativity = 2.16) than Ti (electronegativity = 1.54). Thus electronegativity difference of Mo (2.16) and O (3.44) atom in the Mo-O bond will become lesser which is expected to reduce the band gap of the resulting solid solution [128]. Moreover, Mo-substitution will induce minimum lattice distortion in PbTiO_3 due to the similar ionic radii and almost same first four ionization potentials for Mo and Ti [129].

Incorporation of transition metal Mo is aimed to shift the absorption edge and to inhibit the rate of recombination process of photo generated charge carriers [130, 131]. It is also reported that Mo-doping can promote the densification in NiTiO_3 by reducing the grain size [132]. Creation of defects within the lattice was observed due to Mo doping in NiTiO_3 leading to reduction in average grain size [132]. Mo is also reported to replace Ti easily without requirement of any extra thermal treatment during sample preparation [129]. In the present work, different concentrations (2.5%, 5%, 7.5% and 10%) of Mo-substituted PbTiO_3 were synthesized by high energy ball milling process, and influence of Mo-substitution on the structural, optical and ferroelectric properties were investigated. To the best of our knowledge, such a work was not reported, in the existing literature.

It is well known that dense pellets of PbTiO_3 ceramics are difficult to prepare because of anisotropic lattice expansion at cubic to tetragonal phase transition (at 490°C), during cooling process after sintering, due to large tetragonality (c/a ratio = 1.065) of crystal structure. Elongation of lattice parameters during phase transition

generates large internal stresses, producing fragility and ultimately numerous micro-cracks appear in the ceramics, deteriorating its properties [15] [133]. To overcome this problem, compositional modifications are done to decrease the tetragonality so that ceramic samples can be synthesized by conventional solid-state process. The anisotropic stress arising due to lattice elongation can also be effectively buffered by relaxation provided from increased amount of grain boundaries (making fine particles by high energy Ball milling etc.), and then one can achieve crack-free denser PbTiO_3 ceramic sample.

3.2. Experimental

Ceramic samples of $\text{Pb}(\text{Mo}_x\text{Ti}_{1-x})\text{O}_3$ denoted as MPT were prepared by solid state ceramic method. The samples were denoted as MPT2.5 for $x = 0.025$, MPT5 for $x = 0.05$, MPT7.5 for $x = 0.075$ and MPT10 for $x = 0.10$. For mixing of the reactant powders, Retsch PM400 MA high energy ball mill was used at 300 rpm. Sample to ball weight ratio was taken to be 1:10 for preparation of 10g for all the compositions. Two compositions were also prepared using low energy ball milling process to compare the results with the high energy ball milled samples. Stoichiometric amounts of analytical reagent (AR) grade PbO (Hi-media, 98%), TiO_2 (Sigma Aldrich, 99%) and MoO_2 (Sigma Aldrich, 99%) were ball milled in ethanol (Merck, > 99%) medium for 8 hours. PbO was taken 2% extra to compensate for the Pb-loss during heat treatment of the samples. The milled mixture was dried at 120°C on hot plate to evaporate ethanol. Dried samples were calcined in a muffle furnace for 6 hours at optimum calcination temperature of 950°C . The calcined powders were pressed into pellets with the help of 2% PVA binder at 7 ton pressure. Pellets were sintered at 1050°C temperature in close crucible atmosphere having sacrificial PbO to compensate for the Pb-loss. We could obtain non fragile relatively dense sintered pellets with density ~90%. Thermal reaction

and other thermal changes in samples during heat treatments were investigated in the temperature range 40-800°C at the heating rate 10°C/min by combined thermogravimetric and differential thermal analyzer (TGA-DTA) from Mettler-Toledo. Phase purity of samples were checked by x-ray diffraction studies in the 2θ range 10°-120° at the 2θ steps of 0.02° using Cu-target Rigaku Miniflex x-ray powder diffractometer. Rietveld refinements were performed for structural analysis using FullProf suite [134]. Diffuse UV-Vis spectra of powder samples in reflectance mode were recorded by the SHIMADZU UV-2600, UV-Vis spectrophotometer to estimate the band gap. For surface morphology characterization, microstructure images were taken by scanning electron microscopy (ZEISS EVO 18). KEYSIGHT-E4990A impedance analyzer was used to measure temperature dependent dielectric behaviour. Radiant Precision Premier II ferroelectric tester was used to trace PE loop of all the compositions. Thermo Fisher Scientific (K-alpha) XPS is used to determine the valence states of Pb, Ti, Mo and Oxygen. The average crystallite sizes of all the calcined nano-powders were obtained by using Debye Scherrer's equation [115, 116] $D = \frac{K\lambda}{\beta \cos \theta}$ where β is full width at half maxima (FWHM) [117] of the most intense Bragg peak in the XRD pattern, K (= 0.90) is the shape factor, θ is the Bragg angle, λ is the wavelength of incident X-rays. [135]

3.3. Results and discussions

3.3.1 TGA/DTA Analysis

Fig. 3.1 shows the simultaneous TGA-DTA curve of the uncalcined samples (ball milled mixture of PbO, TiO₂ and MoO₂) of PMT2.5, PMT5, PMT7.5 and PMT10. Two stage decomposition reactions overlapping each other contributing to total loss about 6% were observed in the TGA curve for all the compositions. DTA curve in all the figures shows exothermic peaks at 260°C, 335°C with weight loss and broad peak at

530°C without weight loss. Formation of defect species (vacancies of Pb or Oxygen) might be responsible for this weight loss in TGA curve.

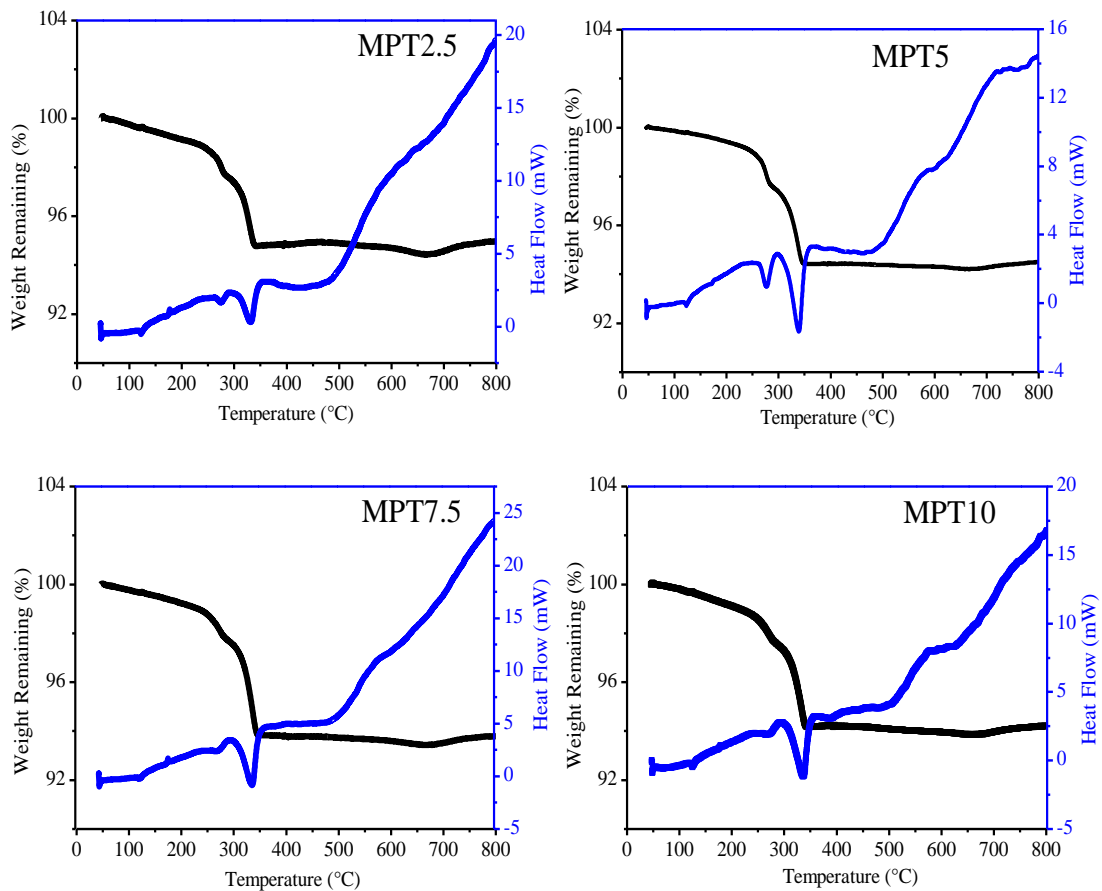


Figure 3.1: Thermo-gravimetric (TGA) and Differential thermal analysis (DTA) curves of MPT2.5, MPT5, MPT7.5 and MPT10 uncalcined samples.

First exothermic DTA peak which is very weak in intensity and corresponding weight loss at 260°C can be attributed to removal of residual ethanol (milling media) remained after drying the sample at hot plate during the synthesis process. The second exothermic peak and significant weight loss at 335°C illustrates solid state reaction of reactant powders accompanied with release of oxygen excess and initiation of crystallization. Change in oxidation state of Mo from +4 to +5 or +6 [129] may cause the creation of Pb vacancies leading to the weight loss around 350°C. Broad exothermic peak around 450°C-550°C without weight loss can be claimed responsible for phase formation/tetragonal to cubic phase transition. Similar thermal behaviour were also

observed in other PbTiO_3 solid solutions [136, 137]. The small increment in mass at higher temperature can be justified by buoyancy effect.

3.3.2 XRD Analysis

X-ray diffraction patterns of two compositions MPT2.5 and MPT10, prepared by low energy ball milling (LBM) and high energy ball milling (HBM) processes are shown in the **Fig. 3.2(a)**. X-ray diffraction patterns of all the four samples reveal a tetragonal crystal structure similar to pure PbTiO_3 (JCPDS card no 06-425). Small impurity peak of PbMoO_3 (JCPDS Card no 44-1486) is also present in the samples prepared by LBM process. The intensity of the impurity peak is negligible for the samples prepared by HBM process. Presence of very weak impurity peak in **Fig. 3.2(a)** for HBM samples shows better dissolution of Mo by high energy ball milling. This is further evident from the lower angle shift (increase in lattice parameter) of the most intense (101) XRD peak for the HBM samples as shown in **Fig. 3.2(b)**. The ionic radius of Mo^{4+} (0.65Å for oxidation state +4 and coordination number 6) and Mo^{5+} (0.61Å for oxidation state +5 and coordination number 6) are slightly larger than Ti^{4+} (0.605Å for oxidation state +4 and coordination number 6) and its substitution can increase the lattice parameters. Average crystallite size of the calcined samples calculated using Scherrer's formula [115], was obtained to be 74.35 nm for low energy ball milled MPT2.5 sample and 52.23 nm for high energy ball milled MPT2.5 sample. Thus, synthesis of MPT via HBM produces relatively pure phase and smaller crystallize size than LBM. In view of this, all the compositions of the samples for further studies were prepared by HBM process. **Fig. 3.2(c)** shows the X-ray diffraction pattern of MPT2.5, MPT5, MPT7.5 and MPT10 prepared by high energy ball milling process calcined at 950°C for 8 hours. All the compositions are seen to be pure perovskite phase with tetragonal structure similar to pure PbTiO_3 . Incorporation of Mo is expected to increase

the unit cell volume and lattice parameters because ionic radii of $\text{Mo}^{4+}/\text{Mo}^{5+}$ is larger than Ti^{4+} .

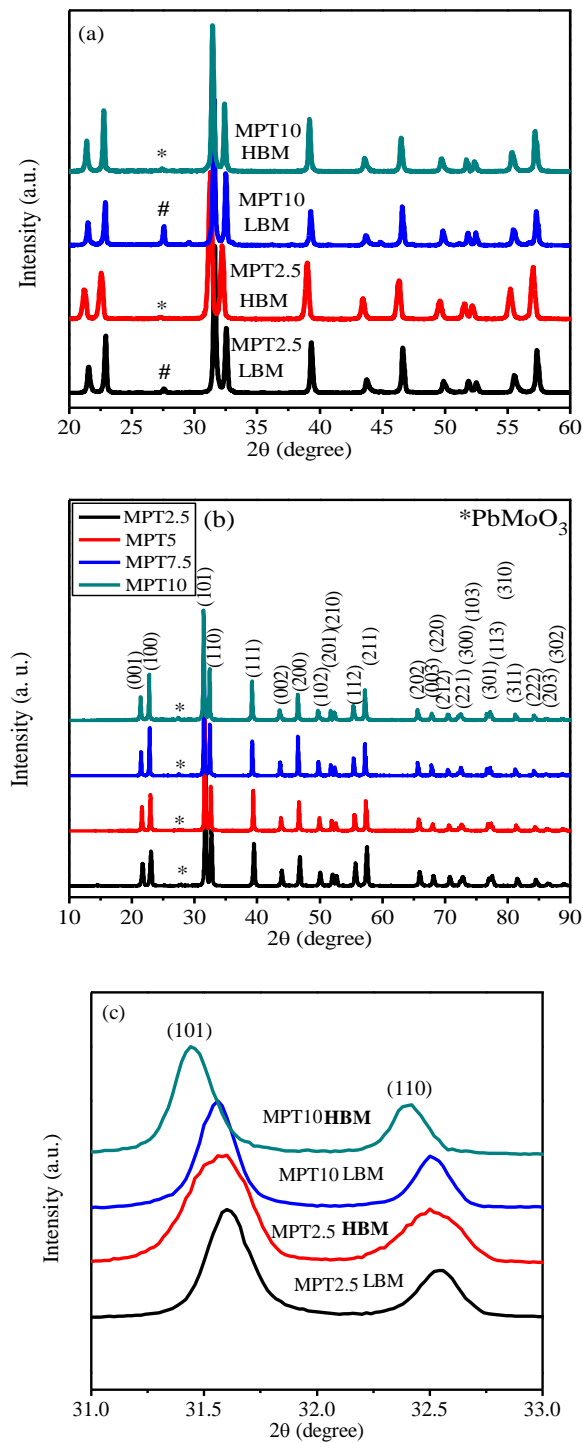


Figure 3.2: (a) X-Ray Diffraction Pattern of MPT2.5 and MPT10 samples prepared by low energy and high energy ball milling processes. (b) X-ray diffraction pattern of

MPT2.5, MPT5, MPT7.5 and MPT10 calcined at 950°C for 8 hours prepared by HBM process (c) shift in the (101) and (110) XRD peaks in the different synthesis processes

Increase in Mo-substitution concentration shows further shifting of the (101) and (110) diffraction peak towards lower angles showing enlargement of both the lattice parameters 'a' and 'b' which was further determined precisely by Rietveld structure refinement. Similar trends were observed when Ti (0.605Å) was substituted by a higher radius atom Zr (0.72 Å) in TiO₂ [138].

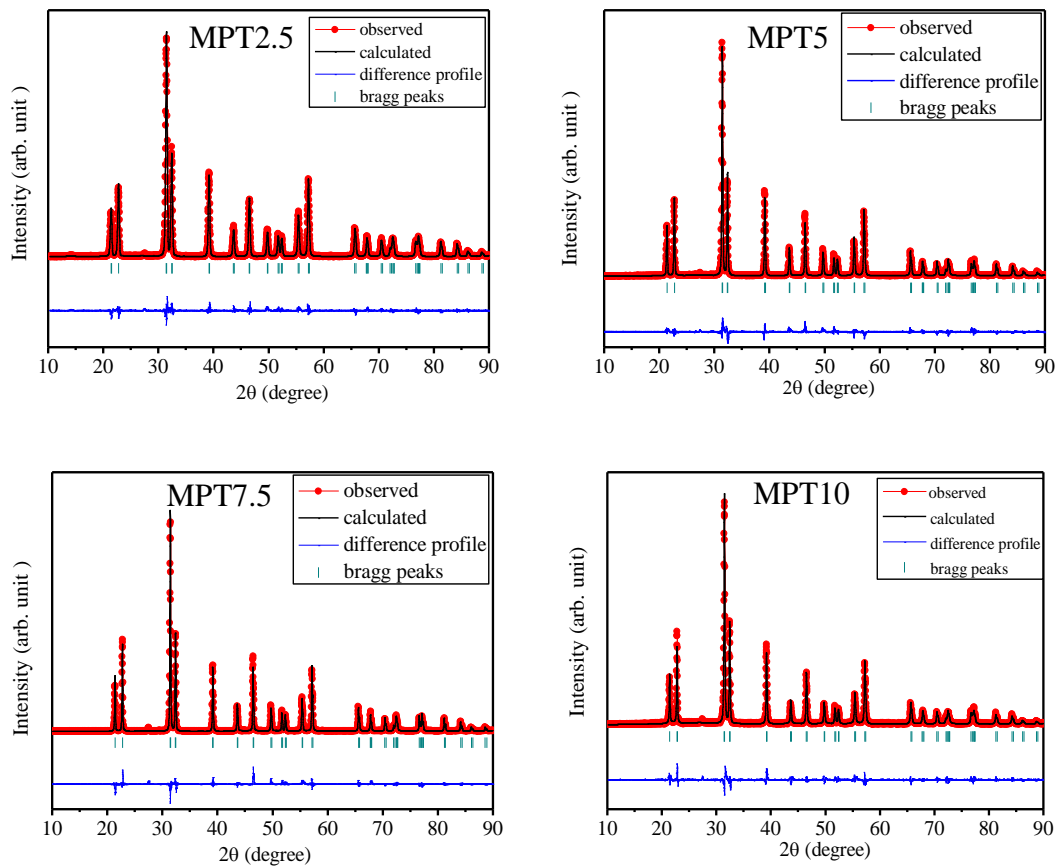


Figure 3.3: Rietveld refinement fits for X-Ray diffraction pattern of MPT2.5, MPT5, MPT7.5 and MPT10. Experimentally observed XRD pattern is shown by red dots overlapping calculated pattern by continuous black line and difference of the two profiles by bottom continuous blue line. The position of Bragg's peaks is symbolized by vertical bars just above the difference profile

Since the structure of various MPT compositions is isostructural to PbTiO_3 , Rietveld structure refinement for all the compositions were performed using tetragonal $P4mm$ space group. **Fig. 3.3** shows a very good Rietveld fit for the XRD pattern of all the compositions except a weak PbMoO_3 impurity peak at $2\theta = 27.43^\circ$, which is barely visible. The values of the refinement agreement factors are also satisfactory as listed in **Fig 3.1**.

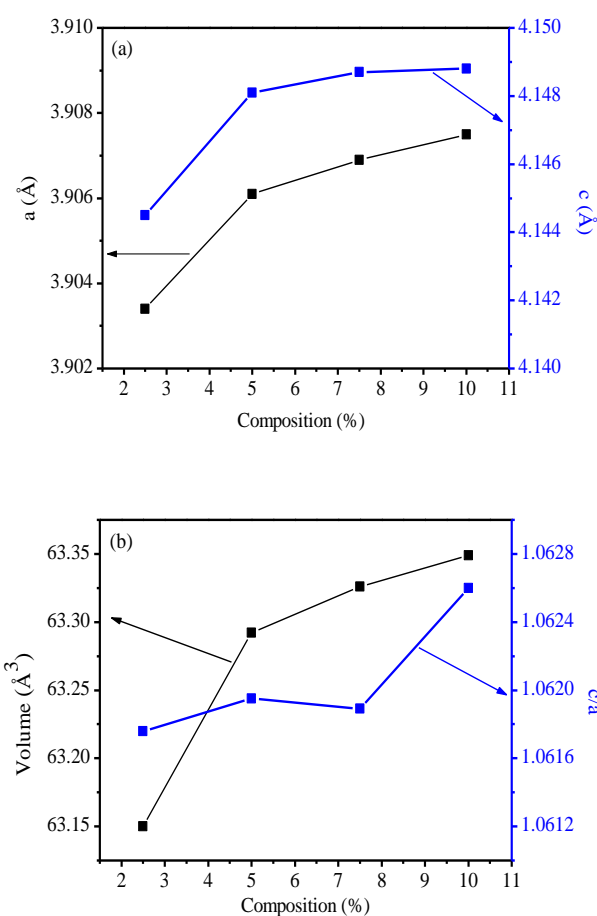


Figure 3.4: (a) Variation in unit cell parameters 'a' and 'c' (b) Change in c/a ratio with increasing Mo concentration for MPT samples.

Table 3.1 lists the lattice parameters, unit cell volume, corresponding density and refined agreement factors obtained from the Rietveld structure refinement for different compositions. Composition dependent variation of lattice parameters, unit cell volume and c/a ratio have also been shown graphically for more obvious representation

in **Fig. 3.4(a)** and **3.4(b)**. The Refined unit cell parameters ‘a’ and ‘c’ for MPT10, are found to increase from 3.8987 to 3.9076 and from 4.1380 to 4.1488 respectively, in comparison to pure PbTiO_3 [139]. Enlargement in ‘c’ is greater than ‘a’ giving rise to higher tetragonality for MPT10. This shift of tetragonality has a scaling with average displacement of Mo/Ti-cation as it was observed earlier in other PbTiO_3 -derived ferroelectric solid solutions [140]. Displacement of Ti/Mo, planer Oxygen(O_{II}) and apical Oxygen (O_{I}) for various MPT samples has been shown in **Table 3.2**. Gradual increase in theoretical density can be attributed to substitution by relatively heavier cation Mo^{4+} (Atomic Weight = 95.95) in place of Ti^{4+} (47.87) while size difference (ionic radius difference~0.045 Å) not being so large.

Table 3.1: Structural parameters and agreement factors obtained after Rietveld structure refinement for MPT2.5, MPT5, MPT7.5 and MPT10.

Composition	MPT2.5	MPT5	MPT7.5	MPT10
Lattice parameter a (Å)	3.9034(1)	3.9061(1)	3.9069(1)	3.9075(1)
Lattice parameter c (Å)	4.1445(1)	4.1481(1)	4.1487(1)	4.1488(1)
Volume (Å ³)	63.150	63.292	63.326	63.348
R_{exp}	10.73	11.67	10.94	13.67
R_{wp}	13.8	17.3	16.7	20.1
χ^2	1.65	2.21	2.33	2.16
RF Factor	1.776	3.178	2.976	2.344
Theoretical Density (g/cm ³)	8.00	8.013	8.040	8.069

Table 3.2: Displacement of ions in various compositions of MPT.

Composition	$\Delta\text{Ti/Mo}$	$\Delta\text{O}_{\text{I}}$	$\Delta\text{O}_{\text{II}}$
MPT2.5	0.036(1)	0.103(2)	0.106(2)
MPT5	0.037(1)	0.096(3)	0.103(2)
MPT7.5	0.039(1)	0.124(3)	0.108(2)
MPT10	0.050(2)	0.083(6)	0.103(4)

It is important to note that the tetragonality of MPT2.5, MPT5, MPT7.5 and MPT10 has not decreased than pure PbTiO_3 even after Mo substitution. In fact, tetragonality

increases with greater addition of Mo concentrations. Lattice distortion with B-site cation Ti/Mo for all substituted samples is observed to be higher than the distortion in pure PbTiO_3 (0.0301\AA) [139]. This suggests that the ferroelectric polarization in Mo-substituted samples will be higher than the pure sample and can give better photovoltaic performance.

3.3.3 Microstructural Analysis

Fig. 3.5 shows the microstructure of sintered ceramic pellets for MPT2.5, MPT5, MPT7.5 and MPT10 respectively, recorded at same magnification. In most of the samples, agglomeration of particles leading to large grains is seen with non-uniform microstructure. However, relatively more uniform grain size distribution is observed in MPT5. Generally, agglomeration is observed when particle size of the ceramic powder used in cold compaction before sintering is too small. In the High energy ball milling process, we obtain very fine particles possessing high surface energy. Minimization of this mechanically introduced overall surface energy and grain boundary energy leads to the agglomeration of the particles. Large grains ($\sim 1.8\text{-}2.3\ \mu\text{m}$) in the sintered pellet are surrounded by smaller grains ($\sim 0.8\text{-}1.0\ \mu\text{m}$) with high crystallinity, as no amorphous phase is seen in the microstructure of all the four compositions shown in **Fig. 3.5**. It is evident from **Fig. 3.5**, that size of even the larger grains is well below the critical size ($\sim 3\ \mu\text{m}$) to obtain crack free pellets, satisfying the criteria to compensate the internal stresses generated during cubic to tetragonal phase transition. Some residual porosity can be seen in all the compositions which is undesirable to obtain a compact and dense pellet [133, 141, 142]. Irrespective of Mo substitution, we observed more or less similar grain size distribution in all the samples, which is in accordance with the results reported for other Mo- substituted systems.

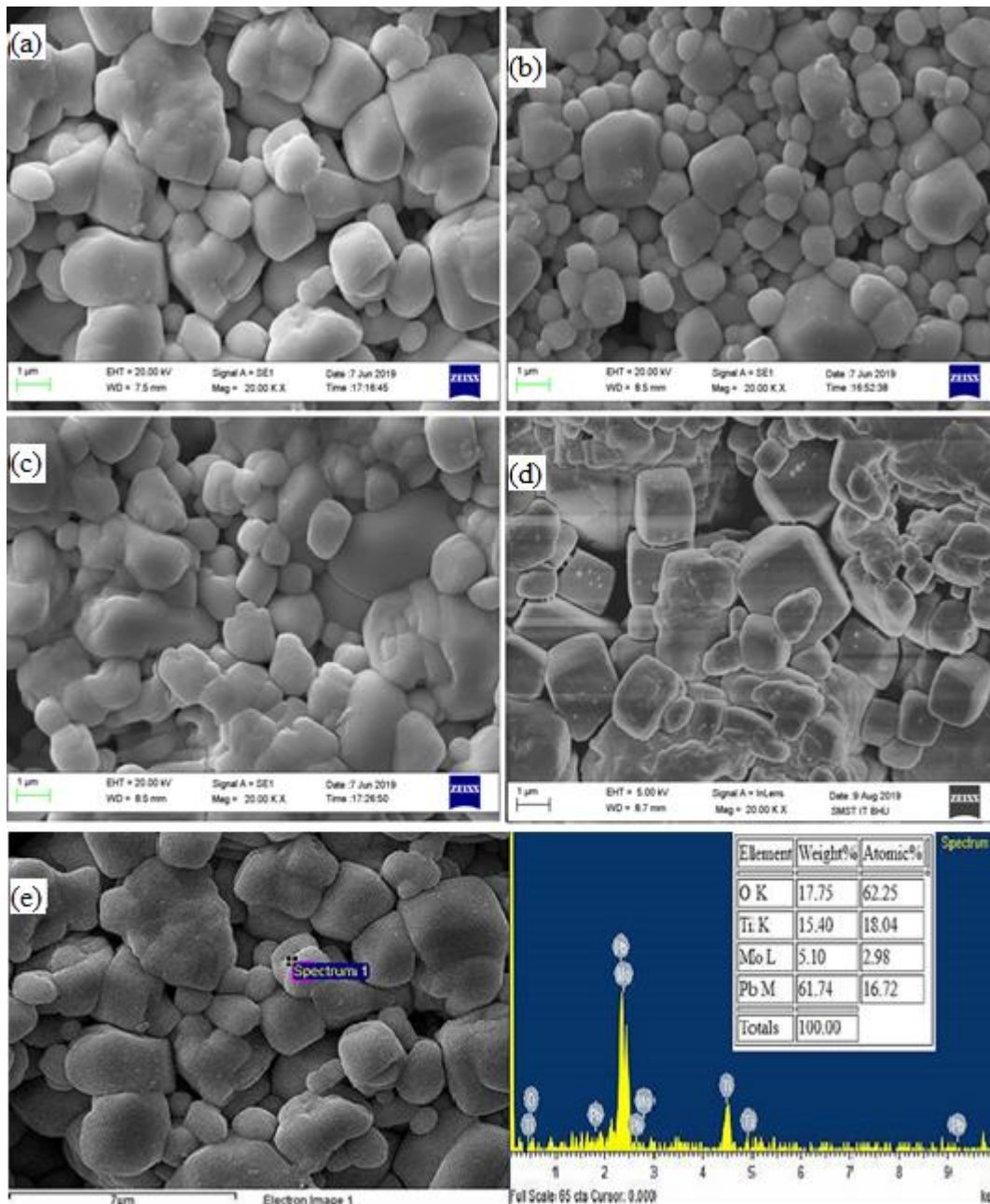


Figure 3.5: SEM image of the MPT pellets sintered at 1050°C for two hours (a) MPT2.5, (b) MPT5, (c) MPT7.5 and (d) MPT10 (e) SEM image and EDS spectra of MPT2.5

Fig. 3.5(e) shows the EDS spectra of the least Mo- substituted sample MPT2.5. It is evident that EDS spectrum shows the presence of expected major elements Pb, Ti and O along with the minor element Mo which confirms the presence of Mo element even in

the least substitution sample. The atomic ratios obtained from the EDS analysis are matching to the nominal composition within the limit of experimental errors.

3.3.4 Band Gap Analysis

Band gaps of the MPT2.5, MPT5, MPT7.5 and MPT10 samples were estimated with the help of Kubelka-Munk function calculated from UV-Vis reflectance spectra plotted against energy, as shown in **Fig. 3.6(a)** [127, 143]. Mathematical relation used for band gap estimation can be expressed by the equation below:

$$(\alpha h\nu)^n = A(h\nu - E_g)$$

where α , $h\nu$ and E_g are absorbance, photon energy and direct band gap energy respectively. 'A' is band tailoring constant and 'n' is exponent which equals 2 for direct band gap estimation. The intersection point of the energy axis with tangent to the linear section of the curve after the inflection point, gives the estimated value of band gap. The band gaps corresponding to MPT2.5, MPT5, MPT7.5 and MPT10 are estimated to be 2.93, 2.64, 2.48 and 2.41 eV respectively which is fairly consistent with the previously reported bandgap [144] where different synthesis process in milling (LBM) was adopted. **Fig. 3.6(b)** shows the composition dependent variation of the band gap for various substitution concentrations of Mo in PbTiO_3 . Band gap for pure PbTiO_3 is reported to be more than 3 eV lying in the UV range [54, 127]. Shifting of band gap from the ultra violet region to the visible region is observed after Mo incorporation. It is evident from the **Fig. 3.6(b)** that composition dependence of band gap adopts a nonlinear variation with an initial steep decay and then gradually reaches at the verge of forming a plateau. Similar decrease in the band gap with Mo substitution were earlier reported in Mo doped anatase TiO_2 . The band gap decreases monotonically from 3.16 eV (pure TiO_2) to 2.73 eV (2.0 % Mo doped TiO_2) with Mo doping in TiO_2 [129]. Our results are consistent to the reports by Zheng, et. al. [15] and W. Zhou et. al. [127]

where, 5% and 33% of transition metal Ti was substituted by Ni in PbTiO_3 , respectively. Substitution by 5% Ni showed the band gap reduction upto 2.53 eV whereas 2.42 eV band gap was observed for 33% Ni incorporation in PbTiO_3 . The mechanism behind this effective reduction of band gap is the gradual decline of the conduction band minima with increasing amount of Ni replacing Ti in PbTiO_3 [15, 127].

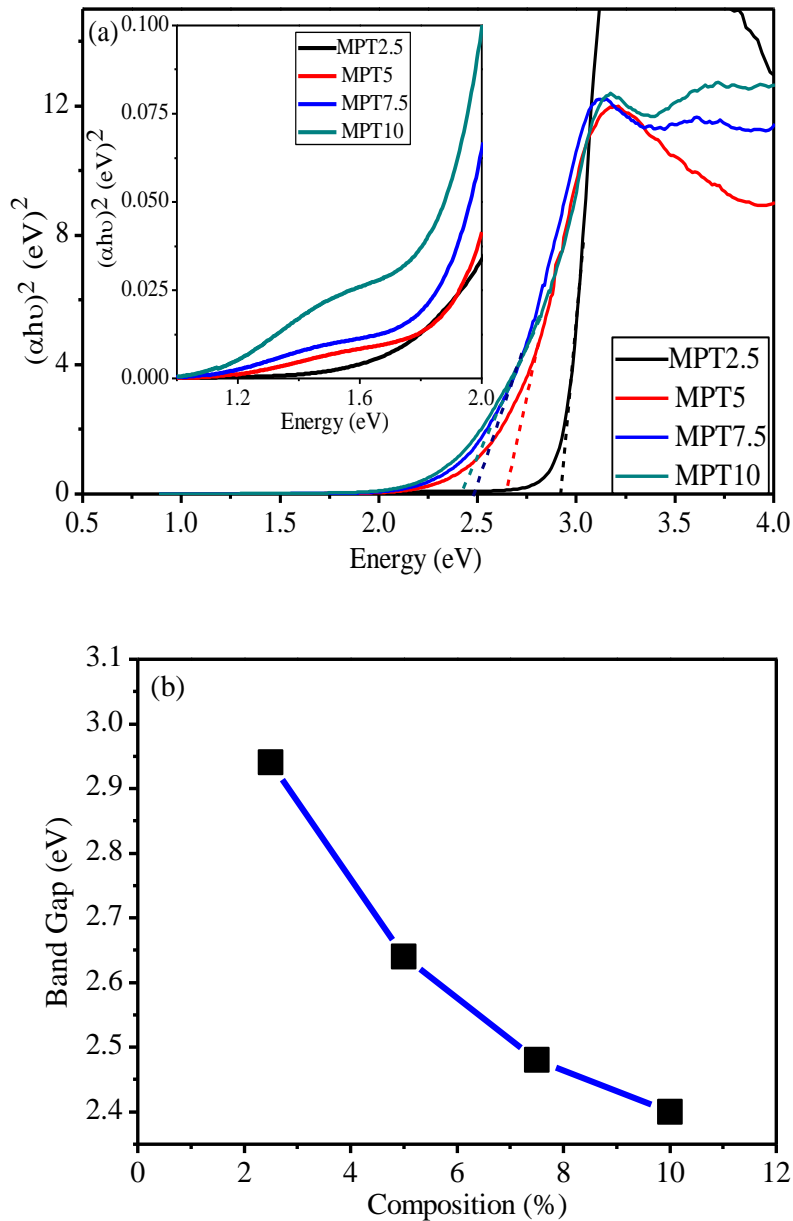


Figure 3.6: (a) $(\alpha h\nu)^2$ versus photon energy ($h\nu$) curve for estimation of the band gap.

(b) Variation of band gap with Mo- substitution concentration in PbTiO_3 .

The decrease in the band gap of PbTiO_3 after Mo- substitution can be attributed to the creation of new states in the electronic structure of both the highest occupied molecular orbital (localized around O-2p) and lowest unoccupied molecular orbital (Localized around Ti-3d). When Mo replaces Ti, the Mo-d states are expected to fall in between the band gap of PbTiO_3 , reducing the band gap of the Mo substituted PbTiO_3 . According to earlier reports in literature, Mo-4d states are lower in energy than Ti-3d states and introduces an impurity state just below conduction band edge extending this band to lower energy and effectively narrowing the band gap. Mo-substitution shifts the fermi level towards bottom of conduction band from top of the valence band thereby showing n-type nature after Mo-substitution [129, 145]. The reduction in band gap may also be related to the relatively high diffuseness of the Mo-4d state than Ti-3d states, as 3d state is smaller in size than size of 4d states [54]. Low energy and weak absorption shown in inset of **Fig. 3.6(a)**, corresponding to energy range 1 eV to 2 eV covering infrared region, may correspond to the transition between the different energy levels of the conduction band after absorption from Mo-4d to Ti-3d states. Mo-substitution introduces impurity states just below the conduction band. Thus, electronic transitions will take place from O-2p to Mo-4d states which is the nearest unoccupied states available. Ti-3d and Mo-4d both are part of conduction band so the transition between them is referred to be as intra-band transition [129].

3.3.5 XPS Analysis

X-ray photoelectric spectroscopy (XPS) has been used to investigate the valence states of the various elements in MPT10 sample. The XPS spectra of Pb, Ti, Mo and O ions are shown in **Fig. 3.7**. The observed XPS spectra for elemental survey confirm the electronic transitions corresponding to Pb, Ti, Mo and O ions while no additional spectrum are seen ruling out presence of any impurity element. Fitting and

deconvolution of experimentally observed peaks were done with the help of XPS peak fitting software XPSPEAK41. As shown in **Fig. 3.7(a)**, scan of Pb-4f shows two peaks at binding energy 136.74 eV and 141.57 eV assigned to $\text{Pb}^{2+} 4f_{7/2}$ and $\text{Pb}^{2+} 4f_{5/2}$. The scan for Ti-2p shown in **Fig. 3.7(b)** also exhibit two peaks at 456.76 eV and 462.55 eV corresponding to $\text{Ti}^{4+} 2p_{3/2}$ and $\text{Ti}^{4+} 2p_{1/2}$ respectively. According to earlier reports [146, 147], incorporation of Mo may shift the binding energy of Ti and Pb due to complex interaction between substituting element Mo and Pb, Ti and O. Due to small amount of substitution, the intensity count in the XPS spectrum of Mo is obtained to be very weak as shown in **Fig. 3.7(c)**. Thus, the results for Mo-XPS spectra should be treated with caution. The XPS spectra peaks shown in **Fig. 3.7(c)** for MPT10 require 4 peaks corresponding to electronic transitions at energies 230.50 eV, 231.04 eV, 233.37 eV and 234.04 eV. These transitions were identified to correspond to the presence of two states of the Mo as Mo^{4+} and Mo^{5+} with $\text{Mo}^{4+} 3d_{5/2}$ at 230.50 eV, $\text{Mo}^{4+} 3d_{3/2}$ at 231.04, $\text{Mo}^{5+} 3d_{5/2}$ at 233.37 eV and $\text{Mo}^{5+} 3d_{3/2}$ at 234.04 eV. The area under curve for Mo^{4+} state is seen to be larger than that for Mo^{5+} which suggests that Mo^{4+} ionization state is in major proportion. Oxidation state of Mo in the precursor used is Mo^{4+} and presence of binding energy peaks corresponding to Mo^{5+} oxidation state shows partial conversion of Mo^{4+} state into Mo^{5+} state during heat treatment of the sample. It is reported earlier in case of TiO_2 that substitution by Mo (Mo^{6+} state in precursor) either substitutes Ti^{4+} in lattice or resides at the interstitial sites in the form of Mo^{4+} , Mo^{5+} and Mo^{6+} [129]. The O 1s spectrum shown in **Fig. 3.7(d)** for MPT10 can be fitted by three peaks as O_I , O_{II} and O_{III} centred at binding energies 528.27 eV, 529.63 eV and 531.23 eV. O_I peak is assigned to lattice oxygen, O_{II} is attributed to vacancies in metal oxide matrix and peak O_{III} relates to the adsorbed oxygen at the surface. It is obvious that intensity of O_{II} peak is very

weak in comparison to peak O_I of lattice oxygen indicating that vacancies are nominal and most of the oxygen are occupied at the lattice sites.

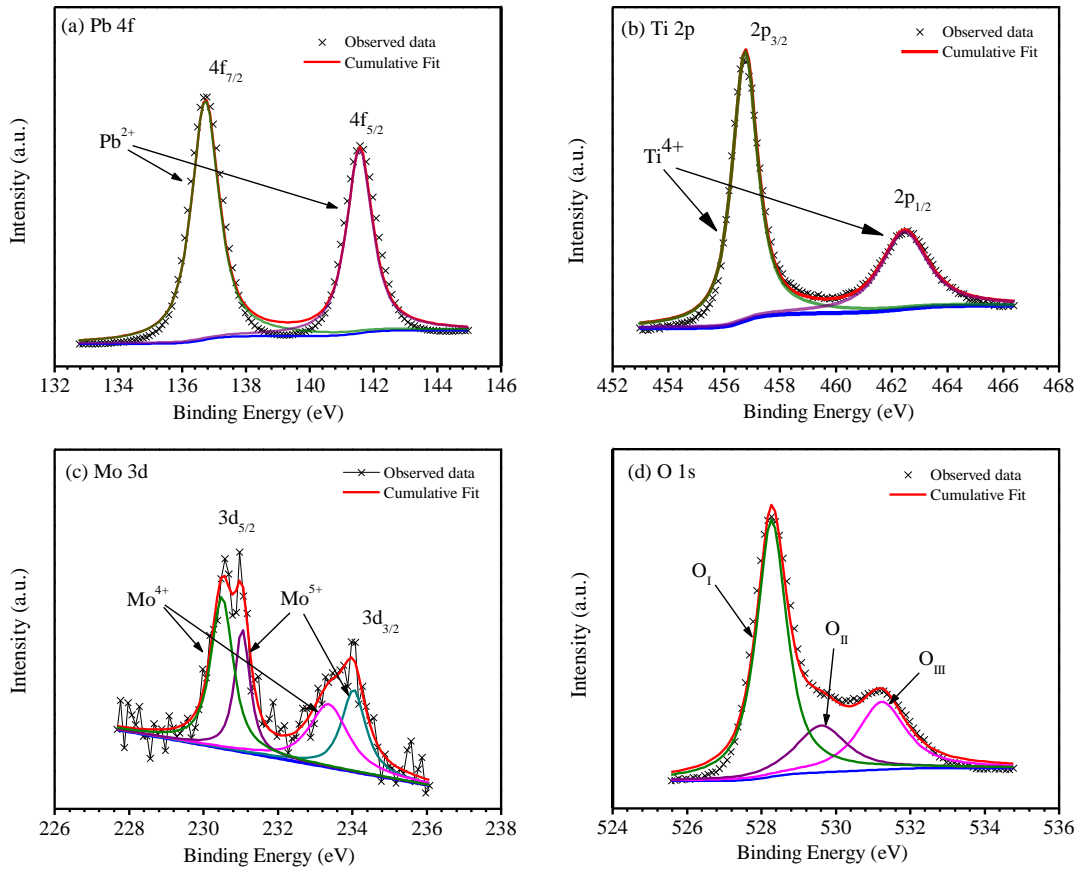


Figure 3.7: Core level XPS spectrum of (a) Pb-4f, (b) Ti-2p, (c) Mo-3d and (d) O-1s for MPT10. (Black cross: observed data; overlapping red line on data: cumulative fit curve; blue line: background baseline; olive, purple, magenta and cyan lines: identification peaks)

3.3.6 Dielectric Analysis

Dielectric characterization of the samples was accomplished by parallel plate capacitor method in the temperature range 40-600°C and frequency range 100Hz-1MHz through a programmable furnace at a heating rate of 2°C/min in the heating run. Temperature-frequency dependent variation of dielectric permittivity (ϵ_r) and dielectric loss ($\tan\delta$) for MPT2.5, MPT5, MPT7.5 and MPT10 are shown in Fig. 3.8(a) and Fig.

3.9, respectively. Both ϵ_r and $\tan\delta$ show decrement with the increase in frequency which is due to relaxation phenomena of dipoles, well explained in known literatures [148].

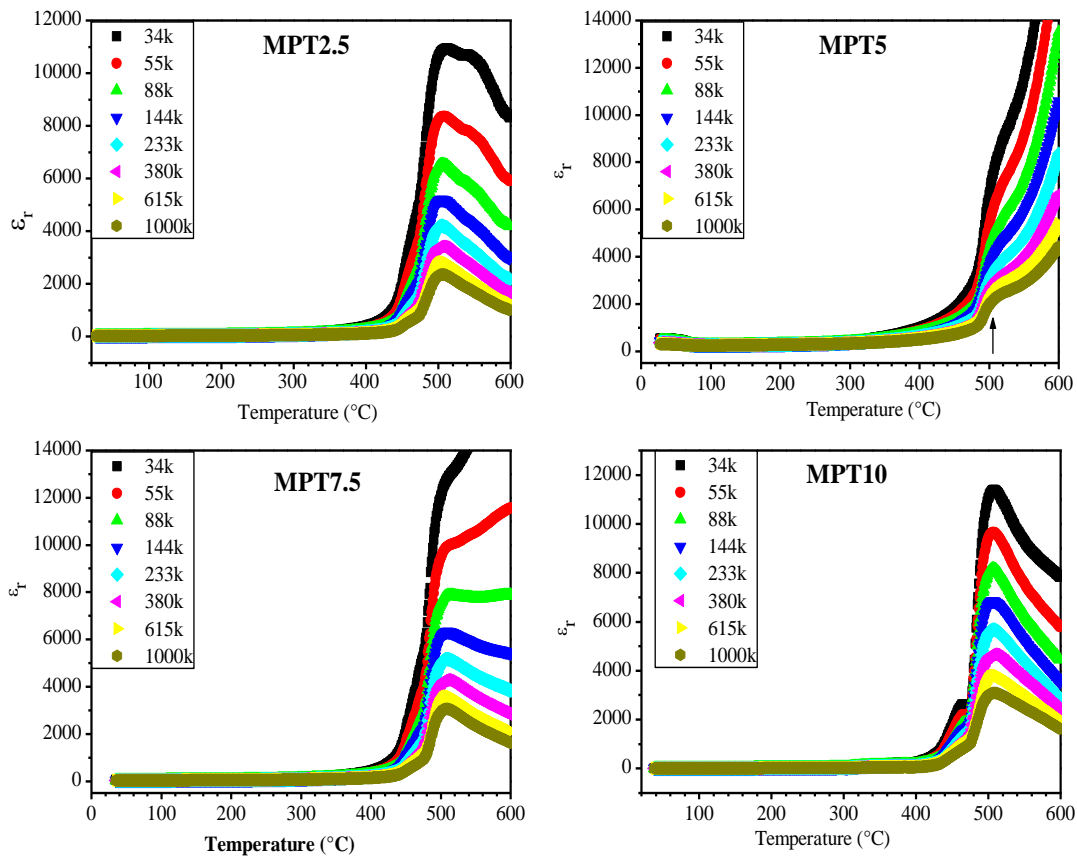


Figure 3.8(a): Temperature-frequency dependence of relative permittivity (ϵ_r) for different compositions MPT2.5, MPT5, MPT7.5 and MPT10.

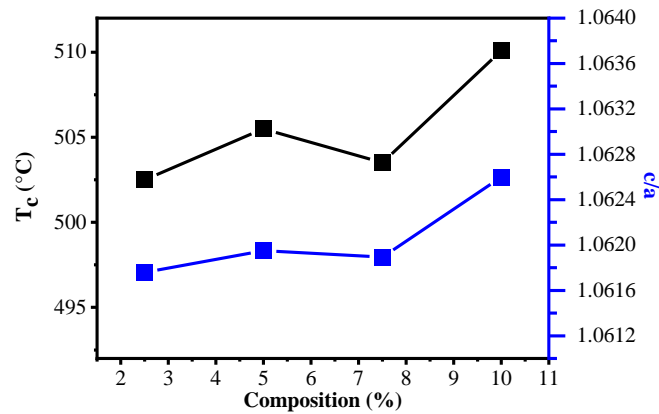


Figure 3.8(b): Variation of T_c and tetragonality (c/a ratio) variation with Mo concentration at the same scale.

A sharp peak in the dielectric permittivity is seen at the ferroelectric transition temperature without peak shift at various frequencies for all the compositions indicating

a non relaxor ferroelectric phase transition at Curie temperature (T_c) similar to that reported for PbTiO_3 at 490°C accompanied with tetragonal to cubic structural phase transition. The sharp transition peaks at the Curie temperature indicates the ordered dipoles within the ferroelectric phase of the material [22, 149]. It is observed that phase transition temperature in all the compositions does not change with the frequency confirming presence of a long range ferroelectric order [22] and absence of any glassy behaviour.

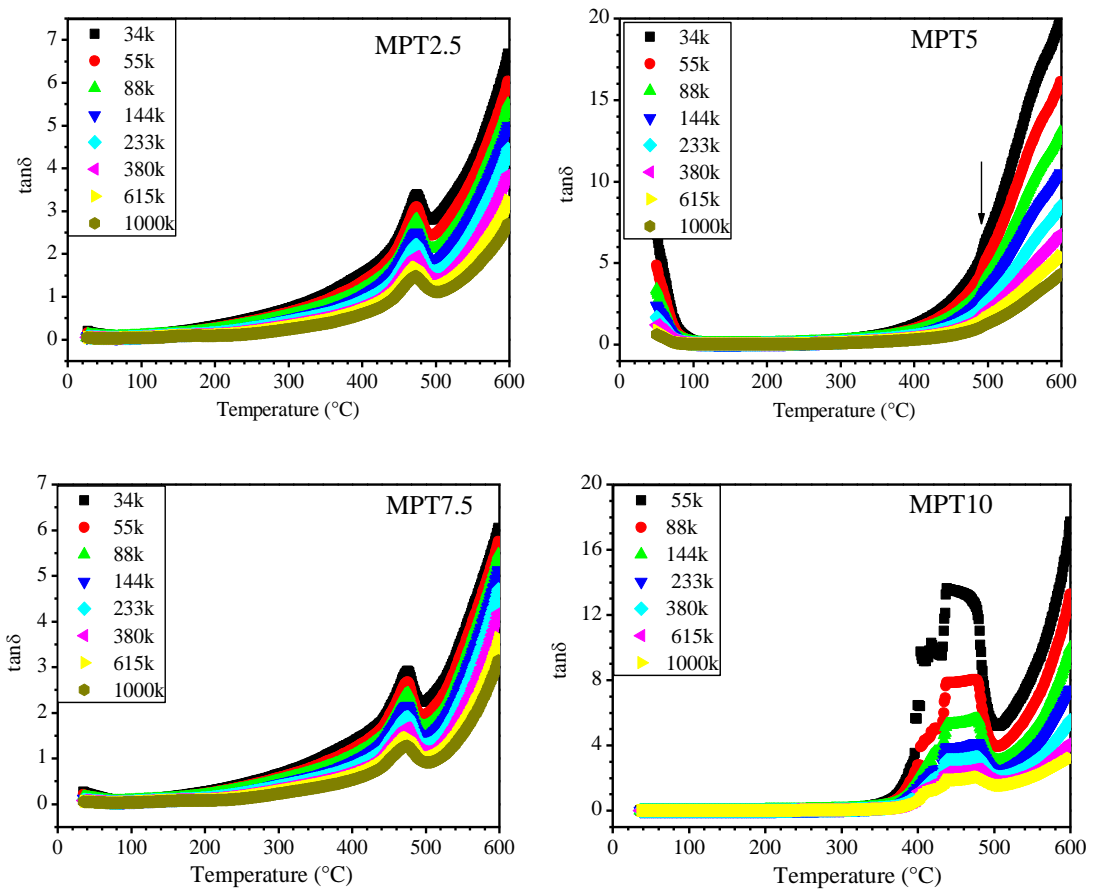


Figure 3.9: Variation of dielectric loss tangent against temperature-frequency for MPT2.5, MPT5, MPT7.5 and MPT10.

However, a slight shift in T_c towards higher value is observed with increasing Mo-concentrations (500°C for MPT2.5 to 510°C for MPT10). This can be attributed to the enhanced tetragonality of the samples for higher substitution concentration of Mo in PbTiO_3 , leading to higher transition temperature which is evident in **Fig. 3.8(b)**. The

dielectric loss in various MPT samples is observed to be low (10^{-1} order) upto 300°C and it increases gradually then sharply as the temperature increases above it. In addition, a peak can be observed around the transition temperature in all the compositions. The dielectric loss peaks are clearly visible in all the compositions except MPT5. In MPT5 sample, only slight turn in temperature dependence of ϵ_r and $\tan\delta$ can be observed at around the transition temperature as marked by arrow in **Fig. 3.8** and **Fig. 3.9**, respectively. This unlike behaviour can be attributed to a different microstructure of the MPT5 pellets which show relatively smaller crystallite size in comparison to other compositions as shown in **Fig. 3.5(b)**. Further, it is observed that for a given frequency, the respective peaks in real part of permittivity (ϵ_r) and loss tangent ($\tan\delta$) are not at the same temperature showing some relaxor nature with disordered structure for various compositions [149]. It can also be seen that loss decreases with the increase of frequency due to dielectric relaxation.

3.3.7 DC Conductivity Analysis:

The most relevant method to observe electrical transport properties in polycrystalline ceramic samples is impedance spectroscopy. Conduction behaviour of MPT2.5, MPT5, MPT7.5 and MPT10 were analysed using impedance spectroscopy over the temperature range 40°C to 400°C and frequency range 100Hz to 1MHz. Typically, ceramics consist of inhomogeneous grains separated by relatively less conducting grain boundaries [150, 151]. Separate contribution of the grains (bulk) and grain boundaries to the total impedance can be estimated by plot between resistive component of impedance (Z') and reactive component of impedance (Z'') i.e., Nyquist plot [150-153]. The Nyquist plots for different composition of MPT samples recorded at room temperature are shown in **Fig. 3.10(a)**. This figure shows Nyquist plot for MPT2.5 recorded at various temperatures. All the plots show semi-circular arcs with its centres

lying on a line below the real axis and starting from the origin and making an intercept on the positive real axis at low frequencies. Single semi-circle arc corresponds to relaxation process in grains only and depressed semi-circle indicates non-Debye relaxation behaviour in which distribution of relaxation time is observed due to inhomogeneities in grain distribution, grain orientation, difference in grain size and atomic defects [152, 154]. In present samples, grain boundary impedance and electrode impedance are negligible and only grain impedance is effective. In Debye type relaxation, semi-circle has centre at the real axis and can be estimated with an equivalent electric circuit having resistance (R_g) and capacitance (C_g) in parallel only. For non-Debye type relaxations, granular impedance can be modelled by using parallel combination of resistance, capacitance and constant phase element (Q) instead of RC circuit as in the case of Debye type relaxation. In our samples, size of the semicircle is correlated to resistance of grains only and size and the number of grains [155] will determine the size of semicircle. **Fig 3.9(a)** shows comparison of experimental complex impedance data with fitted data for MPT for different compositions using the software ZSIMP-WIN version 2. The equivalent fitting circuit is shown in **Fig. 3.10(a)** and **Fig. 3.10(b)** and the fitting grain boundary Resistances (R_b) are listed in **Table 3.3**. Order of fitted capacitance values (C_g) are 10^{-11} - 10^{-10} F, falling in the range of capacitance of bulk ferroelectrics [150]. It can be seen in **Fig. 3.10(a)** that the diameter of the semi-circle decreases with the increase of Mo-concentration up to 7.5% whereas 10% Mo substituted sample shows exceptionally very high resistance. Presence of the relatively larger impurity and non-uniform vacancies which increases impurity scattering of charge carriers, may be the cause of abrupt change in the resistance for MPT10. In **Fig. 3.10(b)**, plots of impedance at different temperatures show reduction in diameter of the semicircle indicating negative temperature coefficient of resistance (NTCR) behaviour.

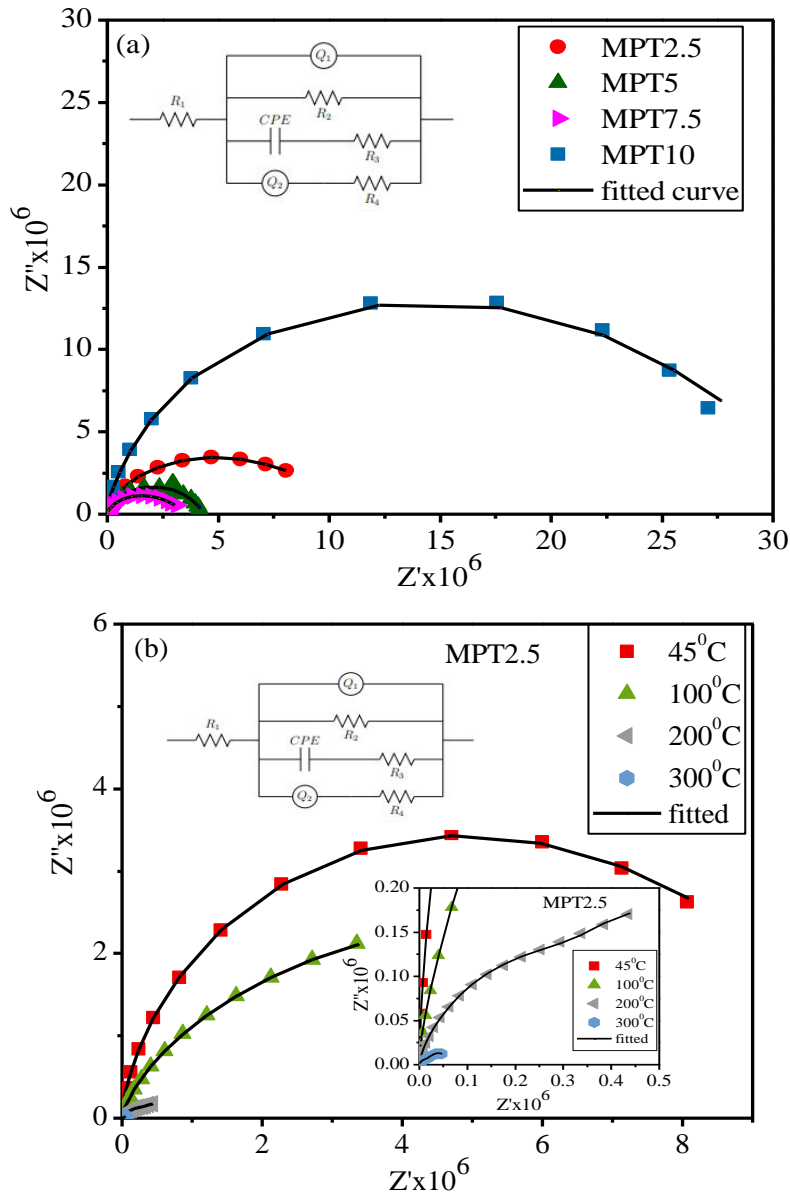


Figure 3.10: (a) Fitted Nyquist plots for MPT2.5, MPT5, MPT7.5 and MPT10 at 45°C.

(b) Fitted Nyquist plot for MPT2.5 at different temperatures, the inset shows the magnified part of Nyquist plot.

Nyquist Plot for MPT2.5 at 200°C and 300°C in **Fig. 3.10(b)** is enlarged and shown in the inset for better visualization. **Table 3.4** lists the DC conductivity of MPT2.5 at different temperature 45°C, 100°C, 200°C and 300°C. The decrease in resistance with increase in temperature shows semiconductor behaviour.

Electrical (DC) conductivity (σ) of the bulk material can be obtained using formula [156] $\sigma = \frac{L}{SR}$ where L represent the thickness, S is the area of the sample and R is the resistance of the grain respectively. Using this formula conductivity of all the four samples were calculated and listed in **Table 3.3**.

Table 3.3: DC impedance and DC conductivity of MPT2.5, MPT5, MPT7.5 and MPT10 at 45°C.

Sample	Resistance $R (x 10^6 \Omega)$	DC Conductivity $\sigma (x 10^{-6} S/m)$
MPT2.5	11.0	1.38
MPT5	4.1	3.68
MPT7.5	3.7	3.95
MPT10	28	0.50

Table 3.4: DC impedance and DC conductivity of MPT2.5 at various temperatures.

Temperature (°C)	Resistance $R (x 10^6 \Omega)$	DC Conductivity $\sigma (x 10^{-6} S/m)$
45	11.0	1.4
100	10.0	1.5
200	0.84	18.1
300	0.07	211.5

It is obvious that increase in Mo-content tends to enhance the conductivity except MPT10 which shows reduced conductivity. Mo is easily oxidizable and oxidation of Mo^{4+} into Mo^{5+} will increase the concentration of carriers. Increased carrier concentration which moves the Fermi level up will favour the band like transport over hopping resulting in enhancement of conductivity because mobility in band like transport is much higher than in hopping [157]. Mo-substitution will insert a doner level below the conduction level reducing the band gap, as estimated well by the UV-vis spectroscopy.

3.3.8 Ferroelectric Analysis

The polarization (P) - electric field (E) hysteresis loop of all the MPT samples measured by Radiant ferroelectric tester at room temperature and up to the 60 kV/cm

field is shown in **Fig. 3.11**. The ferroelectric hysteresis loops on the PbTiO_3 ceramics have not been observed so good as that on single crystal due to low electrical resistivity and high coercive field in polycrystalline samples [158-160]. Optimized poling and improved electrical resistivity are necessary to make the observation of P-E loop possible. The values of polarization observed in the ceramic sample are observed to be small by one order of magnitude as compared with that of single crystal. Similar difference of polarization is also observed in the case of BaTiO_3 . An additional reason might be that in single crystals 180° domain reversal is the main contributor of crystals polarization reversal and no mechanical deformations of the sample is observed along with it. However, in ceramic samples, each grain is mechanically clamped by its surrounding. This clamping effect along with the mechanical stresses associated with 90° domain rotations tries to impede the polarization reversal phenomena as a result increased coercive field (E_c) and low remnant polarization (P_r) are obtained [159]. Ferroelectric hysteresis loop for three compositions (except MPT2.5 due to very high leakage current) MPT5, MPT7.5 and MPT10 shows non-saturated hysteresis loop with slightly decreasing maximum polarization with increasing Mo-content. Further, P_r and E_c shows increasing pattern with increasing Mo concentration. **It can also be observed that shape of loops have started to become rounded at higher Mo concentration.** Non saturated polarization and lossy behaviour at low frequencies may be ascribed to the conduction losses [160, 161]. P_r and E_c values are comparable to the earlier reports of modified PbTiO_3 ceramics [160, 162]. **Fig. 3.11(b)** shows the P-E loop of MPT5 sample recorded at different frequencies. Hysteresis recorded at low frequencies show rounded loops illustrating lossy behaviour of the MPT samples. This roundness can be taken due to high leakage conductivity. Similar behaviour is observed in other samples.

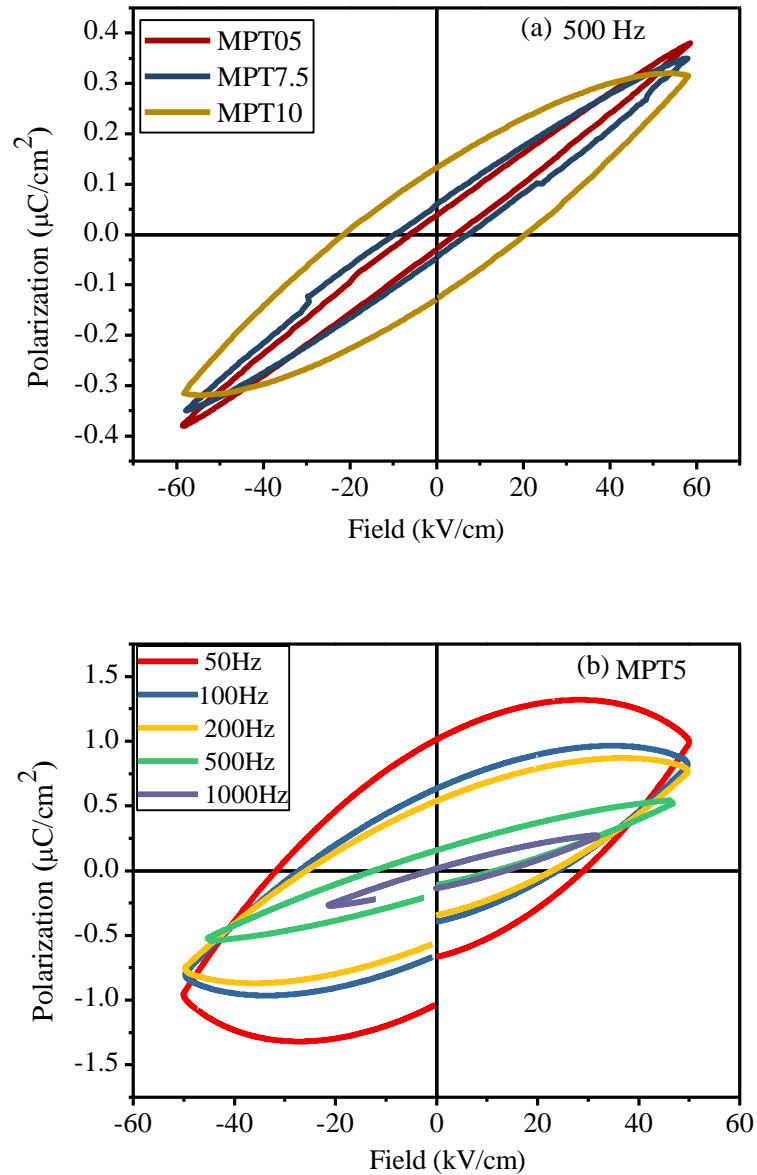


Figure 3.11: (a) Room temperature ferroelectric hysteresis loop of MPT2.5, MPT5, MPT7.5 and MPT10. (b) Room temperature ferroelectric hysteresis loop of MPT5 sample at different frequencies.

If the Ti-ion is substituted with a transition metal having partially filled d-orbital, it tends to suppress the ferroelectric order by forming hybridized states. However larger size of Mo and B-site preference would not only retain geometric distortion but also would enhance it to a small degree. It is well known that Pb-O hybridization plays a crucial role in ferroelectricity of PTO based materials. From the Rietveld refined data, substitution of Mo further shifts the Ti ion from its octahedral centre, hence Ti-3d states

also shift which will change the Ti3d-O2p hybridization, making contribution to larger polarization [163]. In case of PbTiO₃ based solid solutions, it is always difficult to switch the polarization hence measurement of P-E loop is not obtained accurate and well-shaped. However, since tetragonality is rather enhanced polarization is sufficient enough to separate the charge carriers in photovoltaic effect.

3.4. Conclusions

In summary, structural, optical, micro-structural and ferroelectric properties have been investigated on Mo- substituted PbTiO₃ polycrystalline samples synthesized by high energy ball milling process. Structural analysis shows tetragonal perovskite phase of the samples. Rietveld structure refinement from XRD confirms that high energy ball milling process shows better incorporation of Mo than low energy ball milling synthesis process and unit cell parameter changes in such a way that c/a ratio adopts an increasing trend for higher substitution level. Increase in tetragonality (c/a ratio) is also corroborated by the increasing trend in Curie temperature (T_c) determined by temperature dependent permittivity. The microstructure of the sintered samples exhibits agglomerated grains surrounded by pores and non-uniformity in grain distribution, which restricts to get a highly dense and compact pellets. Wide band gap tunability of around 1 eV with Mo-substitution in PbTiO₃ is demonstrated with ferroelectric properties uninfluenced. Conceptually difficult task of shifting the band gap in the visible region without suppressing the ferroelectricity is successfully achieved. Improvement in conductivity is also observed with the increase in Mo-substitution up to 7.5% supporting charge carriers to reach respective electrodes. MPT7.5 which have the band gap of 2.41 eV with better conductivity and sufficient polarization can be considered the most suitable candidate for solar energy harvesting devices.